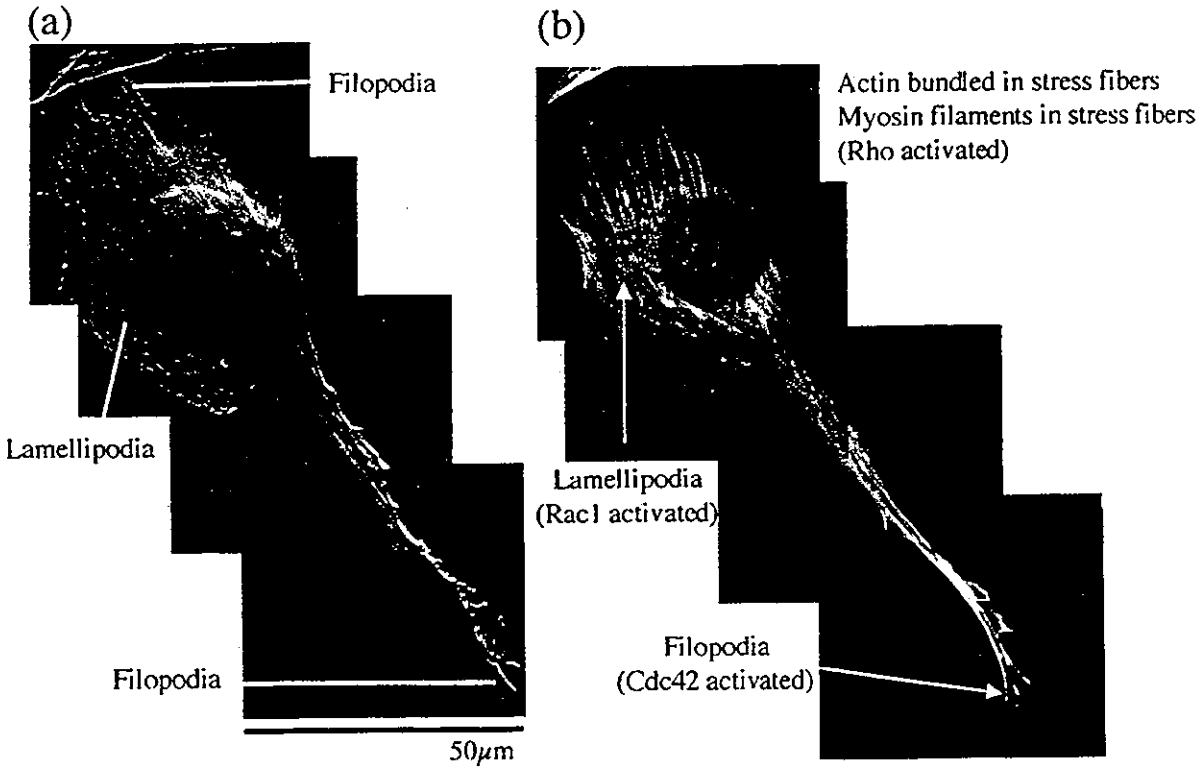

Figure 2. Morphology of lamellipodia and filopodia in a Swiss 3T3 cell adhered to TCPS. Rho activation leads to the assembly of actin-myosin filaments (stress fibers) and of associated focal adhesion complexes. Rac1 activation leads to the assembly of a meshwork of actin filaments at the cell periphery to the lamellipodia and membrane ruffling. Cdc42 activation induces the formation of actin-rich surface protrusions called filopodia. (a) Atomic force microscopy deflection mode image, and (b) fluorescence image of actin cytoskeleton.

them fall into the same cell cycle, GO. The cells were seeded at a density of 2×10^4 cells/cm^2 on respective dishes. The cells were incubated in 10% FCS-containing DMEM medium under the same conditions mentioned above for predetermined period: 0.5, 1, 3, 6, and 24 h.

Immunofluorescence microscopy

Cells were fixed in 10% formalin for 10 min, permeabilized in 0.5% Triton X-100 at room temperature for 5 min, and blocked with 1% bovine serum albumin (BSA) in PBS. The cells were incubated with anti-vinculin monoclonal antibody (at 1:100 dilution; Upstate Biotechnology, NY) in PBS for 1 h at room temperature. After a brief wash with PBS, they were further incubated with a secondary antibody (fluorescein isocyanate–anti-mouse immunoglobulin G at 1:100 dilution; KPL Inc., Gaithersburg, MD) plus rhodamine-phalloidin (at 1:100 dilution; Molecular Probes, Inc., Eugene, OR) in PBS for 1 h at room temperature. Images were acquired using a Bio-Rad Radiance 2000 confocal laser scanning microscopic system (Bio-Rad, Richmond, CA).

Affinity precipitation of Rho, Rac1, and Cdc42

The adhered cells were washed with PBS three times and lysed in RIPA buffer (10 mM Tris-HCl, 150 mM NaCl, 1% Triton X-100, 0.1% sodium dodecyl sulfate, 1 mM ethylenediaminetetraacetic acid, pH 7.4) containing protease and phosphatase inhibitors at the following final concentrations: 1 μg/mL leupeptin, 1 μg/mL aprotinin, 1 μg/mL pepstatin, 1 mM sodium orthovanadate, and 1 mM phenylmethylsulfonyl fluoride. Cell lysates were centrifuged at 1000*g* at 4°C for 10 min and the supernatant was transferred to a fresh tube. Protein concentration was determined by means of the BCA protein assay kit (Pierce, Rockford, IL) with BSA as the standard. Rho activity was determined by the affinity-precipitation method.[18] To determine the activation of Rho, 500 μg of protein (1 μg/μL cell lysate) was incubated with agarose beads conjugated GST-Rho binding domain (RBD) (Upstate Biotechnology) (20 μg) at 4°C for 60 min. The beads were washed three times with cold PBS and boiled in sample buffer. Bound Rho protein was detected by Western blotting using a monoclonal antibody as described below. The amount of RBD-bound Rho was normalized to the total amount of Rho in whole cell lysates for the comparison of Rho activity (level of GTP-bound Rho) in different samples. Values represent Rho activity relative to that of cells at time 0. That is, the time-dependent Rho, Rac1, Cdc42 activities were normalized to those of suspension cells, which were subjected to the serum-starved, staged cells and detached from the dishes before cell seeding. This method did not determine activation of the subset population of the Rho subfamily (Rho-A, -B, and -C). According to the manufacturer's instruction, this method allows precipitation of the

TABLE I
Parameters Characterizing the Movement of 3T3 Cells for 3–5 h and 23–25 h Culture on TCPS, PS, and PET

Parameter	Time (h)	TCPS	PS	PET
Total length of cell trajectory (μm)[a]	3–5	175.39 ± 27.01	200.35 ± 25.53	171.69 ± 15.28
	23–25	189.78 ± 38.34	227.92 ± 31.45	213.36 ± 71.15
Average speed of cell movement (μm/min)[b]	3–5	1.46 ± 0.23	1.67 ± 0.21	1.43 ± 0.13
	23–25	1.58 ± 0.32	1.90 ± 0.26	1.78 ± 0.59
Length of final cell displacement (μm)[c]	3–5	16.55 ± 13.39	30.29 ± 9.90	8.22 ± 3.85
	23–25	27.86 ± 26.82	36.76 ± 26.87	24.39 ± 13.89
Average rate of cell displacement (μm/min)[d]	3–5	0.14 ± 0.11	0.25 ± 0.08	0.07 ± 0.03
	23–25	0.23 ± 0.22	0.31 ± 0.22	0.20 ± 0.12
Coefficient of dislocation efficiency[e]	3–5	0.10 ± 0.09	0.15 ± 0.05	0.05 ± 0.02
	23–25	0.14 ± 0.11	0.16 ± 0.10	0.12 ± 0.07

Values are given as the means ± SD.
[a]Total length of cell trajectory in every 2-min step.
[b]Average speed of cell locomotion defined as total length of cell trajectory/time of recording.
[c]Total length of final cell displacement of the cell from (i.e., distance between) the first and last points of the cell track.
[d]Average speed of cell locomotion defined as total length of cell displacement/time of recording.
[e]The ratio of cell displacement length to cell trajectory length. Coefficient of dislocation efficiency would equal 1 for the cell moving persistently along one straight line in one direction and zero for a random movement..

GTP-Rho (activated) not GDP-Rho (inactivated) at the detection limit of 0.5–2 μg/mL of detected Rho in lysates from the cells. To determine the activation of Rac1 and Cdc42, GST-p21 binding domain (PBD) conjugated agarose beads (Upstate Biotechnology) (10 μg) were used and the Western blotting technique as mentioned below was used. Results are given as means ± standard deviation (SD) of five runs.

Western blotting

Western blots of Cdc42 and Rho were separately run using the respective antibodies. The identification of bands detected was performed using the antibodies included in the commercial kits used. The proteins were separated in 10% sodium dodecyl sulfate polyacrylamide gel and transferred to the polyvinylidene difluoride membrane (Bio-Rad). The membranes were blocked in T-PBS (0.1% Tween 20 with PBS) with 1% BSA. After washing in PBS, the blots were incubated with the primary antibody (1 μg/mL in T-PBS): Rho (Santa Cruz Biotechnology Inc.), Rac1 (Upstate Biotechnology), or Cdc42 (Santa Cruz Biotechnology Inc.) antibody, at room temperature for 1 h. After washing with PBS, the blots were treated with the secondary antibody (1 μg/mL in T-PBS) (fluorescein isocyanate–anti-mouse immunoglobulin G; KPL Inc.) at room temperature for 1 h. Densitometry was performed using the Molecular Imager FX (Bio-Rad). At every measurement, the control was set as the value at time 0, and the value at each measurement was normalized to that of control.

Time-lapse analysis of cell migration

The substrate-dependent migratory behavior of cells was monitored by a time-lapse image-capturing system (HIMAWARI; Library Inc., Tokyo, Japan) connected to a phase-contrast microscope (IX70; Olympus, Tokyo, Japan) with a temperature and humidity controllable cell chamber (MATS-CO2CHK; TOKAI HIT, Shizuoka, Japan). Before the time-lapse recording experiment, cells were seeded at a density of 2×10^3 cells/cm^2 on each substrate and cultured with DMEM containing 10% FCS under 5% CO_2 for 3 or 23 h. Then, DMEM was exchanged with L15 (Gibco BRL) containing 10% FCS. This medium exchange was performed to adapt the cultured cells to the long observation period without needing to regulate CO_2 concentration in our cell chamber. Images of cells were captured every 2 min for 120 min. The coordinates of 10 isolated cells were measured by digitizing software using the position of their nuclei. The migratory track and the moving speed were calculated from the coordinates, and cell trajectories were presented in circular diagrams with the starting point of each trajectory situated in the diagram center. The parameters affecting cell motility were computed for each cell and are tabulated in Table I (definitions of parameters are given in the footnotes).

RESULTS

The adhesion and spreading states at 3 h and 24 h after plating were determined by fluorescence immunohistochemical staining and phase-contrast microscopy. The migratory potentials were time-lapse determined by measuring the time-lapse tracking of moving cells. The activation of Rho families (Rho, Rac1, and Cdc42) was determined by affinity precipitation and Western blotting techniques.

Cell adhesion and spreading

Swiss 3T3 fibroblasts, confluently grown and subjected to an overnight serum starvation before use,

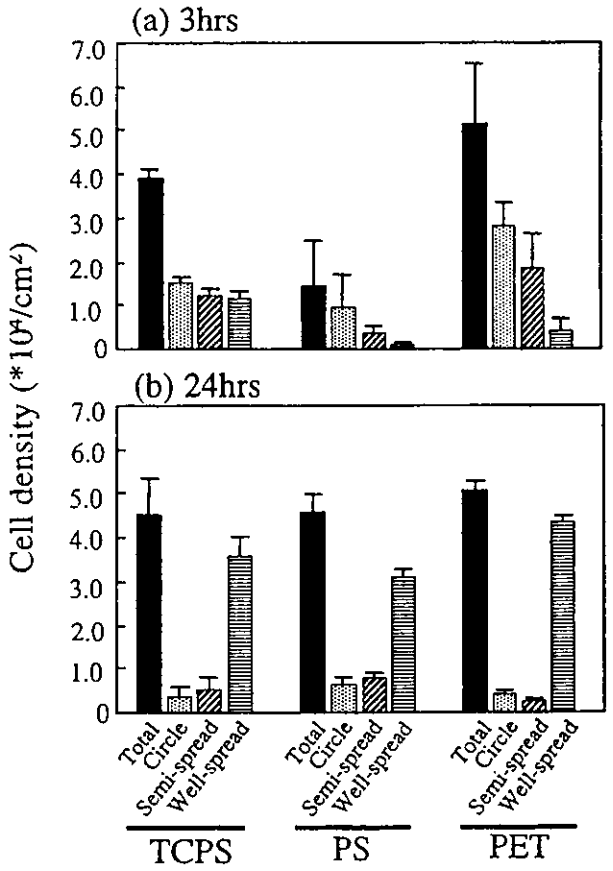

Figure 3. Number of adhered cells and subpopulation of cell shape (nonspread circular shape, semispread, and well-spread) on TCPS, PS, and PET at 3 h and 24 h after plating. At least 300 cells were analyzed at each time point.

were seeded and cultured on three different substrates (TCPS dishes, biological PS culture dishes, and PET film) in the serum-containing medium for up to 24 h. TCPS and PET substrates were selected as substrate characteristics of high cell adhesion and spreading, whereas biological PS was selected as a substrate characteristic of a markedly reduced adhesion and spreading.

The number of cells adhering to these substrates and the cell shape were determined under a phase-contrast microscope at 3 h and 24 h after plating. At 3 h, the number of adhered cells was the highest for PET, followed by that for TCPS, whereas a markedly reduced cell number was noted for PS, which was almost one-fourth to one-third of those on the former two substrates [Fig. 3(a)]. However, there was a marked difference in the spreading state between the three substrates: when cell shapes were roughly divided into three shapes such as circular (or round), semispread, and well spread, cells cultured on TCPS had almost equal subpopulations of these three different shapes. However, for the PET substrate, more than half (55%) of the cells remained round, approximately one-third (37%) had the semispread shape, and a very small population (<10%) had the well-spread shape. A higher subpopulation of round cells (approximately 71%) was found for PS. At 24 h after plating, there was little difference between the subpopulations of cells on TCPS and those on PET [Fig. 3(b)]. Most cells (80–86%) were well spread, and round ones remained <10%. Although the subpopulation of round cells adhering to PS was similar to those on TCPS and PET, the cells comprised <20% of the total populations. These cells were all living ones, which was confirmed by the trypan blue staining method.

Figure 4 shows the substrate-dependent relative occurrence of lamellipodia to total adhered cells. At 3 h, irrespective of type of the substrate, lamellipodia was found in 25–30% of the total cell population. At 24 h, an increased population of lamellipodia was noted in cells grown on all the substrates. Approximately 50–55% of adhered cells on TCPS and PET exhibited noticeable lamellipodia, whereas the subpopulation of cells with lamellipodia on PS remained around 40%.

Cytoskeletal dynamics

The cytoskeletal dynamics of actin stress fiber and vinculin in cells were determined by immunofluorescence microscopy using rhodamine-phalloidin to label α-actin and actin stress fibers, and anti-vinculin antibody to determine focal adhesion or adhesion plaques. Figures 5–7 show the time courses of the formation and distribution of focal adhesion and stress fibers in cells that adhered to these substrates. At 0.5–1 h after plating, regardless of the type of substrate, round cells

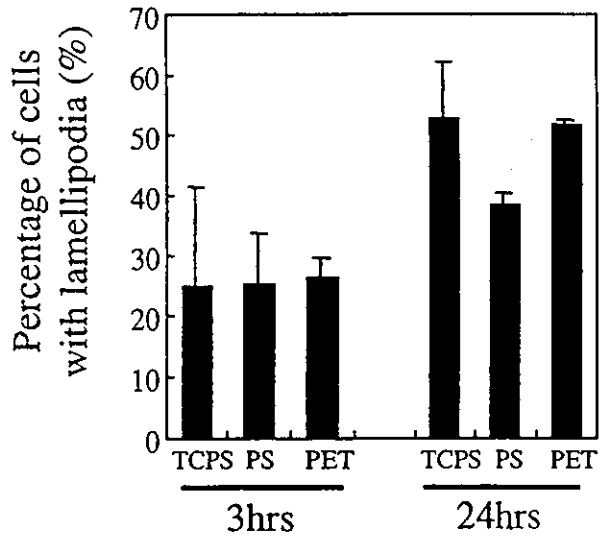

Figure 4. Substrate-dependent population of cells with lamellipodia at 3 h and 24 h after serum-starved cells were plated at a density of 2×10^4 cells/cm^2.

without any signs of spreading were dominant. Vinculin and α-actin were localized at the peripheral regions of adhered cells to form rings. At 3 h, the spreading state depended on the type of substrate: on TCPS, well-spread cells, which comprised almost one-third of the entire population, had actin fibers being developed to form stress fibers and vinculin localized at the front edges of spread cells (Fig. 5). These became more enhanced at 6 h after plating: stress fibers developed to transverse the intracellular space although major actin fibers were still localized at the peripheral regions of cells. Vinculin was distributed in spots at the front edges of peripheral regions as well as the central parts of intracellular regions.

However, on both PS and PET, cells at 3 h after plating did not exhibit any signs of spreading: a large population of round cells was noted (Figs. 6 and 7). At 6 h, the population of spread cells increased on PET, whereas nonspread cells were still dominant on PS. At 24 h after plating, irrespective of the type of substrate, cells were well spread on the substrates and developed prominent focal adhesions that were detected by vinculin staining: many stress fibers terminated at focal adhesions. The cell shapes of lamellipodia and filopodia were observed in these cells.

Cell migration

Cell migration was measured during 3–5 h and 23–25 h after plating. The positions of cells, which were sparsely seeded to reduce the probability of contact with each other, were acquired with a phase-contrast microscope, and images were taken at 2-min intervals during a total observation period of 120 min. Migratory tracks were determined from the positions of cell nuclei digitized on the images at a time interval from which the migration speed was calculated. The following parameters characterizing cell migration were computed for each cell: (a) the total length of cell trajectory, (b) the average speed of cell locomotion defined as the total length of cell trajectory/recording time, (c) the total length of the final displacement of the cell from (i.e., distance between) the first and last points of the cell track, (d) the average speed of cell locomotion defined as total length of cell displacement/time of recording, and (d) the cell displacement length to cell trajectory length, which is also called the coefficient of dislocation efficiency.[19,20] Table I lists these parameters obtained on the three substrates at the periods of 3–5 h and 23–25 h after plating.

Figure 8 shows examples of the migratory tracks (trajectories) of cells on the three substrate surfaces. During the first observation period (3–5 h), random migration of cells was observed on TCPS: cells exhibited membrane ruffling and moved via very frequent cycles of a large extent of expansion and retraction of pseudopods. The moving speed of the cells, calculated from the cell trajectory, was approximately 1.46 μm/min. In contrast, the cells that adhered to PS, on which cells were not spread well, moved by changing cell shape: cells exhibited very frequent cycles of a small extent of expansion and contraction of pseudopodia. The moving speed of the cells was 1.67 μm/min. The cells that adhered to PET appeared to remain at almost the same place: cells exhibited very slight expansion and contraction of pseudopodia at the same place. The moving speed of the cells was 1.43 μm/min. Although the total length of the cell trajectory was not strongly dependent on the type of substrate, both final displacement and the coefficient of dislocation efficiency were found to be the highest for PS, followed by TCPS and lastly, by PET.

However, during the well-spread period (23–25 h after plating), irrespective of type of substrate, the cells on all the substrates moved randomly, and the length of final displacement was considerably increased compared with that in the early period. The total length of the cell trajectory and the average cell migration speed were not significantly increased except for those for PET. On PS substrate, there was significant difference in parameters on cell motility between the early and late periods of observation. However, marked increases in the length of final displacement, the average rate of cell displacement, and the coefficient of dislocation efficiency were noted for both TCPS and PET substrates. These cell motility parameters for TCPS and PET became similar to those for PS at 24 h after plating.

Expressions of Rho, Rac1, and Cdc42

Time courses of Rho, Rac1, and Cdc42 activation during adhesion, spreading, and migration processes were determined by plating serum-starved cells onto each dish. The activities of Rho, Rac1, and Cdc42, determined by the affinity-precipitation method, were expressed as the amount of RBD-bound Rho normalized by the amount of Rho in whole-cell lysates. With the commercially available detection kit used here, only activated forms of the whole Rho subfamily (Rho-A, -B, and -C) were measured. Figure 9 shows the time course of Rho family activity of the cells adhered to the three different substrates. Values represent Rho activity relative to serum-starved cells on the dishes before cell seeding, at time 0. Regardless of the type of substrate, Rho activity increased with incubation time, reaching a maximal value (almost 1.5- to 2.0-fold higher than the basal level) at 0.5–1 h and gradually returning to the basal level at 24 h. This indicates that there is no significant difference in the

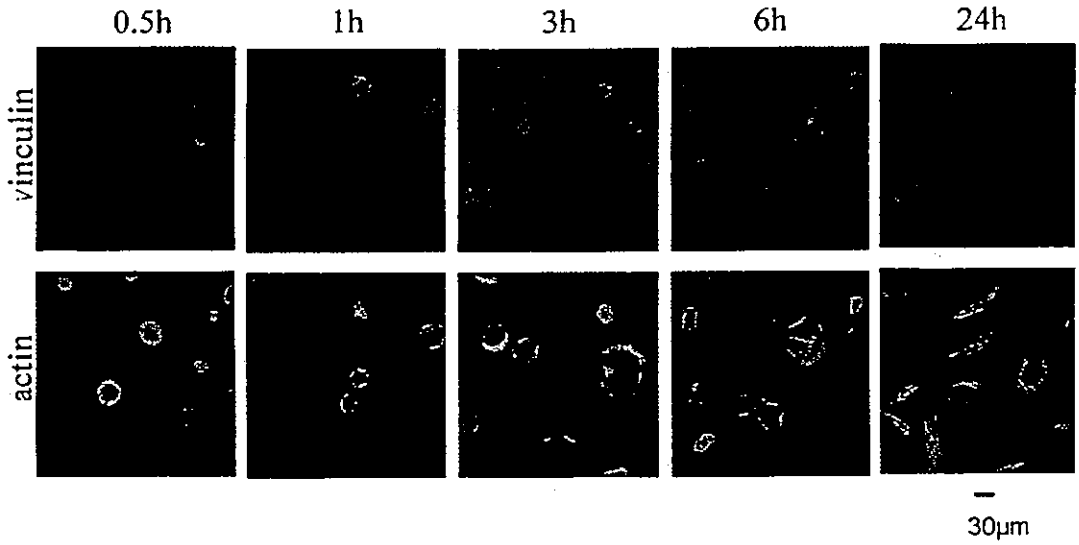

Figure 5.

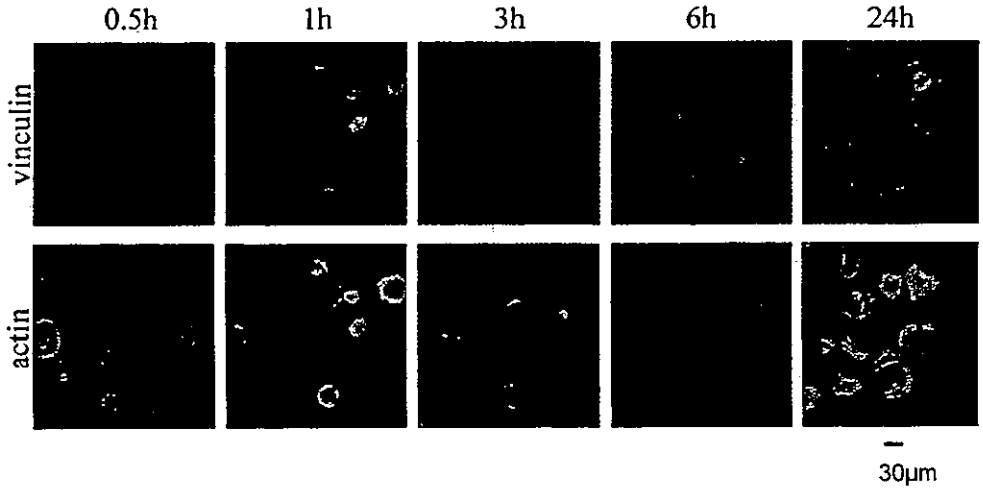

Figure 6.

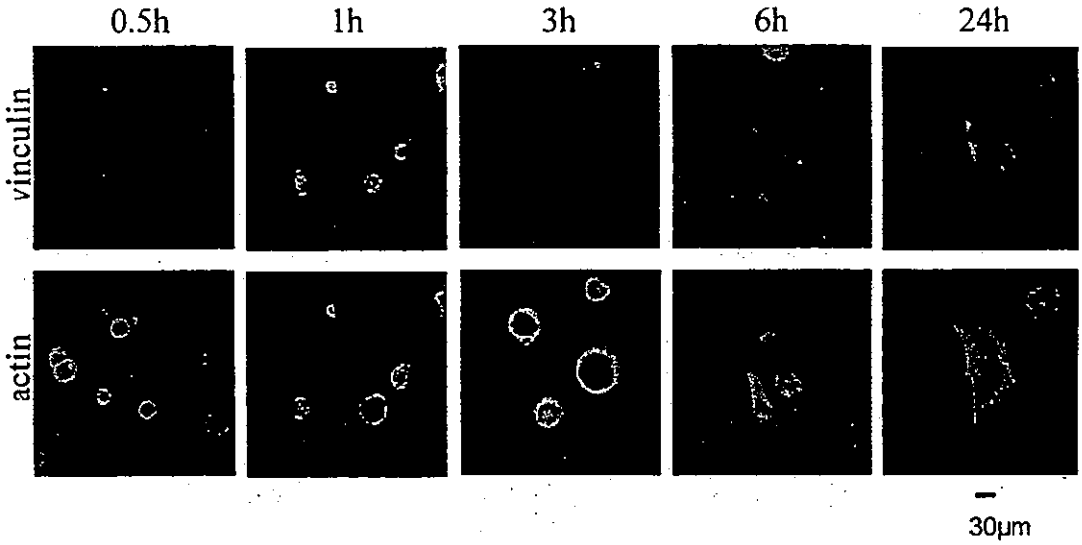

Figure 7.

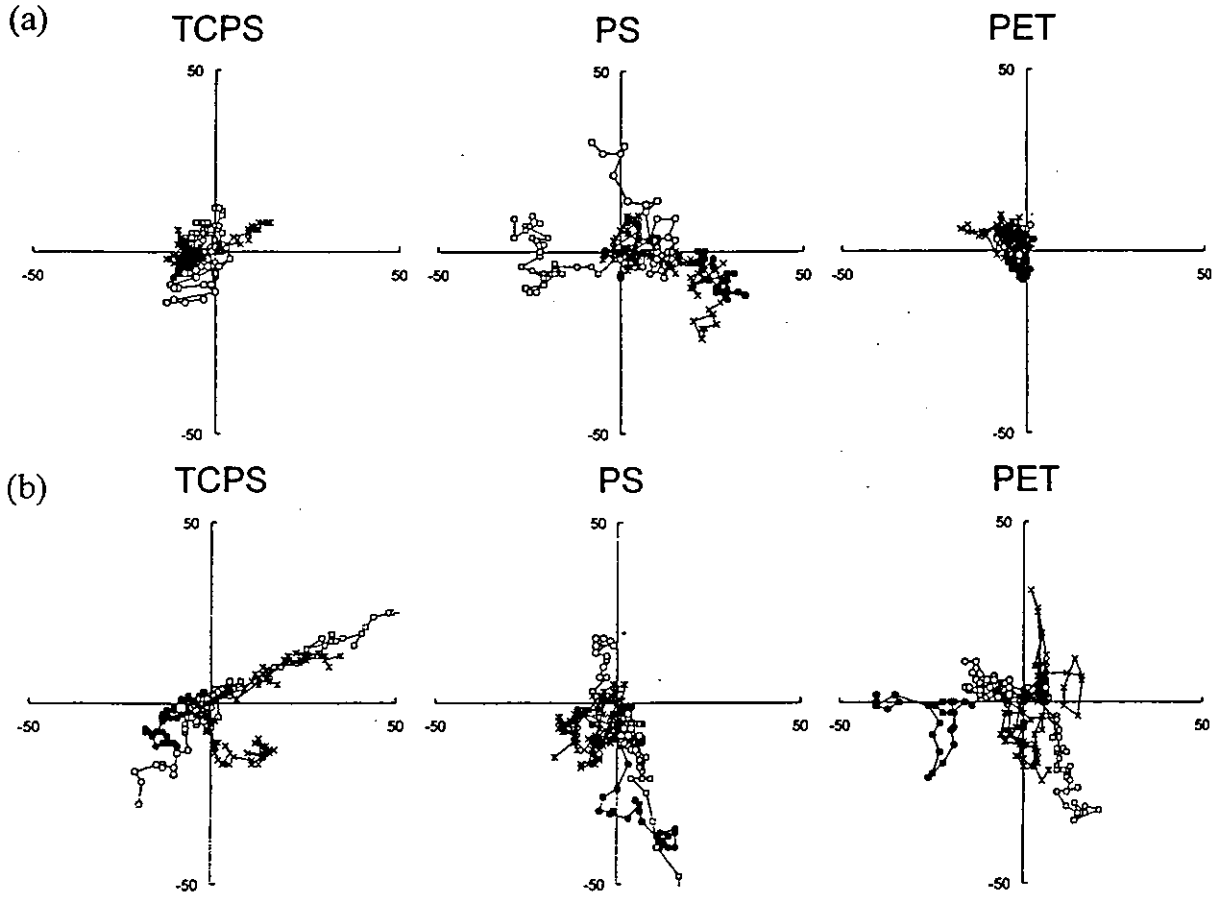

Figure 8. Migratory tracks of Swiss 3T3 cells on TCPS, PS, and PET drawn with the initial point of each trajectory being the origin of the plot. The images were recorded (a) 3–5 h, and (b) 23–25 h. After plating, and the positions of cell centroids were determined at 2-min intervals.

time course of Rho activation among the substrates. Rac1 activity of the cells adhering to TCPS and PET increased within a shorter time (0.5 h) and maintained the same level that was almost 1.4- to 1.5-fold higher than the control. In contrast, Rac1 activity of cells adhering to PS peaked at 0.5–1 h, and then returned to the basal level. Cdc42 activity of cells adhering to TCPS increased within a shorter time (0.5–1.0 h) and maintained the same level (approximately 1.5-fold higher than control) during the observation period. In contrast, Cdc42 activity of cells adhering to PS was very low and appeared to remain at the basal level, whereas that of cells adhering to PET increased within 0.5–1 h and maintained that level (1.2-fold higher than the basal level).

DISCUSSION

Tissue morphogenesis is driven by changes in cell shape, growth, and function that are coordinated in both time and space, and is governed by transmembrane signal transduction in the local tissue microenvironment

Figure 5. Time course of focal adhesion and stress fiber formation in cells adhered to TCPS. Cells were plated onto TCPS at a seeding density of 2×10^4 cells/cm^2. At the times indicated, cells were fixed and actin filaments were visualized with rhodamine-phalloidin, and in the same cells vinculin was localized by immunofluorescence microscopy using mouse anti-vinculin antibody to detect focal adhesions. Bar represents 30 μm.

Figure 6. Time course of focal adhesion and stress fiber formation in cells adhered to PS. The experimental procedure was the same as that in Figure 5.

Figure 7. Time course of focal adhesion and stress fiber formation in cells adhered to PET. The experimental procedure was the same as that in Figure 5.

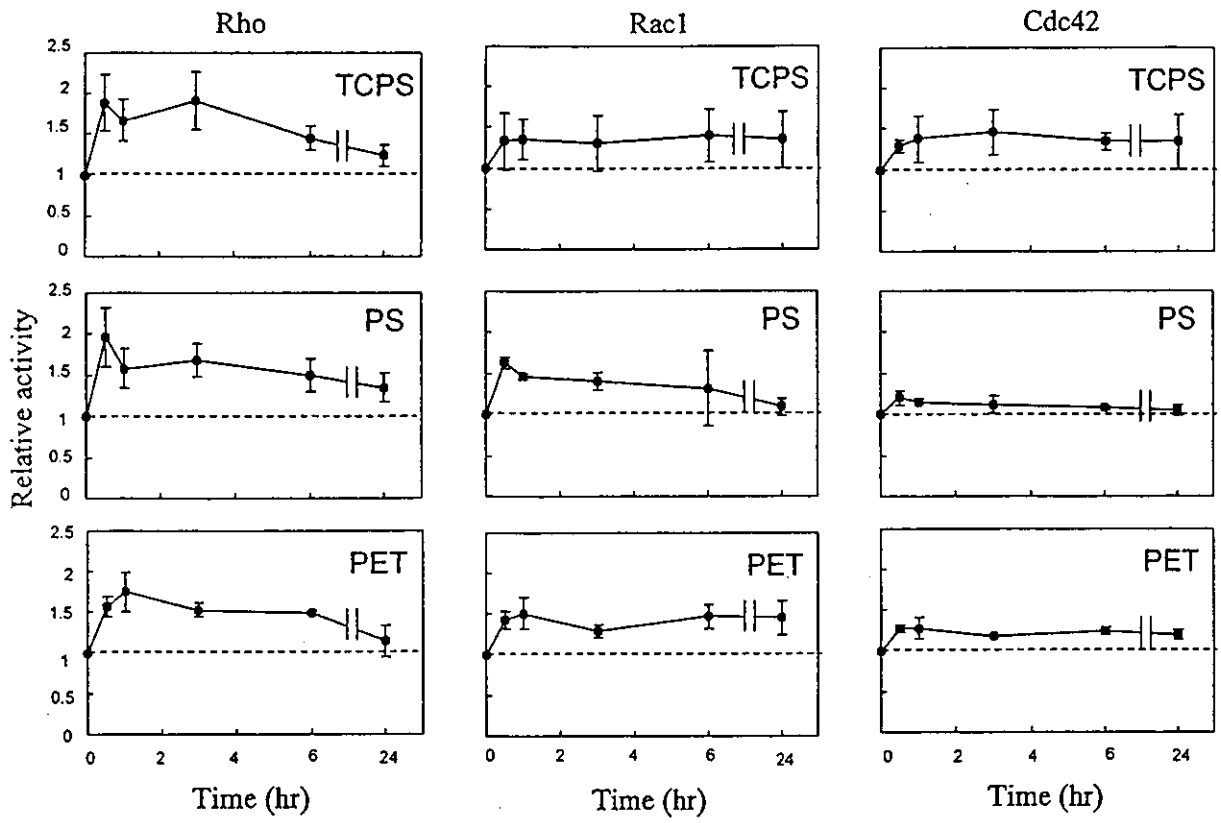

Figure 9. Relative activities of Rho GTPases (Rho, Rac1, and Cdc42) of cells adhering to TCPS, PS, and PET. Values represent corresponding Rho activity relative to serum-starved cells at time 0. Results are means ± SD from five experimental runs.

when stimulated by a variety of environmental cues.[21,22] As schematically shown in Scheme 1, integrin (cell receptor)-adhesive protein adsorbed to a synthetic substrate triggers transmembrane signaling, thereby activating Rho family and integrin clustering.{Scheme1} This induces cytoskeletal organization and the formation of an adhesion machinery as well as the deactivation of Rho (negative control).[23] These changes determine cell shape and morphology as well as cell migration.[24,25] Such sequential molecular events with positive and negative feedback and amplification occur.

In this study, the sequential events in the morphogenesis of cell-lined fibroblasts after plating for up to 24 h on three different substrates were determined. During the first 24 h after plating, various stages of cell behavior, such as macroscopic cell shape and microscopic morphology (lamellipodia and filopodia), cytoskeletal dynamics including stress fibers and adhe-

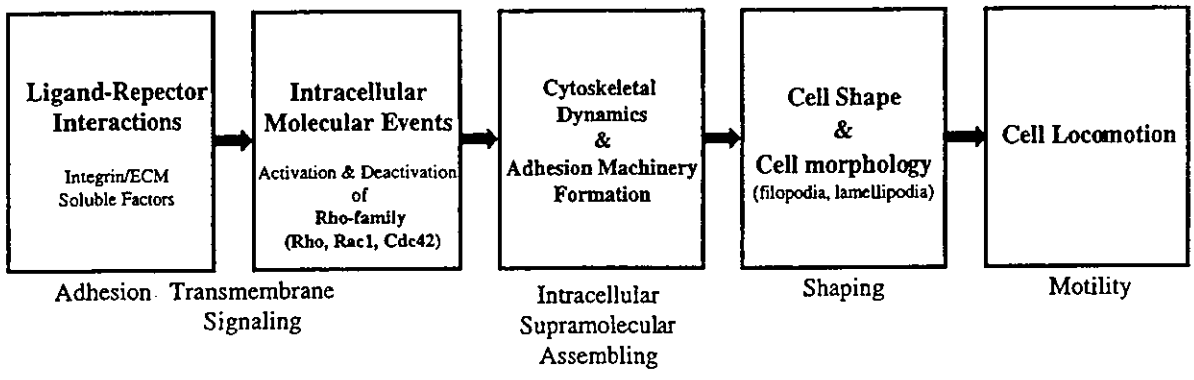

Scheme 1. Sequential molecular and cellular events during the adhesion and spreading processes. ECM, extracellular matrix.

sion plaques, and activation/deactivation of Rho family (Rho, Rac1, and Cdc42) occur simultaneously with culture time. Before the discussion of the Rho activity-cell shape/motility relationship, the experimental results are summarized as follows.

- Adhesion potential: at 3 h, the number of adhered cells was almost identical for both TCPS and PET, whereas that for PS was very small. At 24 h, there was no significant difference in the number of adhered cells among the three substrates.
- Cell shape and morphology: at 3 h, the subpopulation of spread cells was the highest on TCPS, followed by that on PET. Minimal population was noticed on PS, and concomitantly the subpopulation of round (or nonspread) cells was the highest for PS, followed by that for PET, and lastly, that for TCPS. The population of cells with lamellipodia was almost the same at 3 h after plating and increased thereafter irrespective of the type of substrate used. There was some substrate-dependent difference in population at 24 h. The lowest cell population was found for PS.
- Cell motility: the average speed of cell movement was not significantly different among cells on the three types of substrates and the observation periods. However, the length of final displacement, the average rate of displacement, and the coefficient of dislocation efficacy increased at the later period of observation for all substrates. These three parameters were highest for PS, regardless of the observation period.
- Activation of Rho family: Rho activation was maximal at 0.5–1.0 h after plating and gradually decreased thereafter to reach the basal level, irrespective of the type of substrate used. Almost the same level of Rac1 activation was noted during the entire observation period for cells on TCPS and PET (approximately 1.5-fold higher than the basal level), whereas for cells on PS, a maximal level was observed at 0.5 h after plating and continuously decreased to the basal level thereafter. The continuous Cdc42 activation occurred for each substrate, but the degree of activation was the highest for cells on TCPS, followed by those on PET. Minimal activation was found for cells on PS.

From these results, we postulate the following interrelationships between temporal cell shape/morphology/migration and activation of Rho family. Strong adhesivity and rapid spreading, both of which were observed in cells on PET and TCPS, should be caused by the strong interaction between integrin and substrate (via adsorbed protein), which is related to the continuously constant activation of Rac1 and Cdc42. The least adhesive substrate, PS, probably because of the weakest interaction between integrin and proteins on the substrate, continuously decreased Rac1 activation and exhibited very small activation of Cdc42. This may be responsible for the retarded spreading. As for cell motility, cells on PS, the least adhesive substrate, appeared to exhibit the highest motility. Although the formation of pseudopods including lamellipodia and filopodia is required for cell motility, small levels of activation of Rac1 and Cdc42 appear to be beneficial for cell motility because the less spreading cells have lower interaction strength with the substrate. Much literature reported that Rac1 activity enhances cell raffling or microscopic, regional movement at the peripheral region (lamellipodia) of cells. Therefore, we expected that there must be some correlation between motility and Rac1 activity. However, the present study did not provide any correlation. Although we have little rational interpretation on this matter, one possible interpretation is that macroscopic cell movement requires the locomotion of a whole body of cells to which raffling is only partly contributed.

As for the substrate-induced Rho activation, McClay and Grainger[26] first reported in-depth study using two well-defined substrates: one is carboxyl group terminus-bearing self-assembled monolayer (SAM) on gold substrate, and the other is methyl group terminus-bearing SAM, both of which were prepared using corresponding alkanethiol. Their study was focused to activation of Rho-A, which is primarily known for its regulation of cell-surface-induced focal contact and stress fiber formation upon Rho-A-stimulated bundling and contractility of actin-myosin complexes leading to the clustering of integrin receptors. Their findings include that carboxyl group-terminated SAM, on which Swiss 3T3 fibroblasts spread well, enhanced Rho-A activation more than methyl group-terminated SAM, which is a less adherent substrate than the former SAM, whereas the nonactivated GDI-Rho level was much higher for the methyl group-terminated SAM than the carboxyl group-terminated SAM. These results support that surface chemistry greatly influences the activation state of Rho-A. Koenig et al.[27] tried to correlate cell adhesion with Rho-A. Rho-A activation in the nearly confluent, quiescent, nondividing cells on TCPS likely was minimal, whereas the less-adherent Teflon (polytetrafluoroethylene) surface exhibited the highest Rho-A activation, suggesting that survival activity of cells appears to enhance Rho-A activity.[27] The other relating preceding study by Putnam et al.,[28] includes externally applied mechanical forces-dependent activation of membrane-associated Rho-A and Rac: the activation of Rho-A and Rac is increased under compression strain but is decreased under tensile strain,[28] affecting the change in the state of microtubule polymerization. To our knowledge, besides these studies, there is no report to

establish the substrate-dependent relationship between cellular behaviors (cell shape, cell morphology, cytoskeletal architecture, and cell motility) and the activation of the Rho family, which has been recently identified as central coordinators of a remarkable variety of cell functions, as mentioned above. Although a clear-cut relationship between Rho and cell behaviors was not established in this study, the accumulation of more data may define the degree of contribution of Rho activation to these cellular behaviors, which will determine tissue compatibility, tissue morphogenesis, and engineered tissue architecture, all of which are the fundamental basis of artificial implants and tissue engineered devices.[1-4]

References

1. Saltzman WM. Cell interactions with polymers: principles of tissue engineering. Lanze RP, Langer R, Chick WL, editors. San Diego: Academic Press; 1997. p 225.
2. Lackie JM. Cell movement and cell behaviour. London: Allen & Unwin; 1986.
3. Ross JM. Cell–extracellular matrix interactions. In: Patrick CW Jr, Mikos AG, McIntire LV, editors. Frontiers in tissue engineering. Elmsford, NY: Pergamon; 1998.
4. Al-Rubeai M. Cell engineering. Boston: Kluwer Academic Publishers; 1999.
5. Burridge K, Chrzanowska-Wodnicka M. Focal adhesions, contractility, and signaling. Annu Rev Cell Dev Biol 1996;12:463–519.
6. Hall A. Rho GTPases and the actin cytoskeleton. Science 1998; 279(5350):509–514.
7. Schwartz MA, Shattil SJ. Signaling networks linking integrins and rho family GTPases. Trends Biochem Sci 2000;25(8):388–391.
8. Schmitz AA, Govek EE, Bottner B, Van Aelst L. Rho GTPases: signaling, migration, and invasion. Exp Cell Res 2000;261(1):1–12.
9. Zheng Y, Olson MF, Hall A, Cerione RA, Toksoz D. Direct involvement of the small GTP-binding protein Rho in lbc oncogene function. J Biol Chem 1995;270(16):9031–9034.
10. Ridley AJ, Hall A. The small GTP-binding protein rho regulates the assembly of focal adhesions and actin stress fibers in response to growth factors. Cell 1992;70(3):389–399.
11. Hartwig JH, Bokoch GM, Carpenter CL, Janmey PA, Taylor LA, Toker A, Stossel TP. Thrombin receptor ligation and activated Rac uncap actin filament barbed ends through phosphoinositide synthesis in permeabilized human platelets. Cell 1995;82(4):643–653.
12. Ridley AJ, Paterson HF, Johnston CL, Diekmann D, Hall A. The small GTP-binding protein rac regulates growth factor-induced membrane ruffling. Cell 1992;70(3):401–410.
13. Kozma R, Ahmed S, Best A, Lim L. The Ras-related protein Cdc42Hs and bradykinin promote formation of peripheral actin microspikes and filopodia in Swiss 3T3 fibroblasts. Mol Cell Biol 1995;15(4):1942–1952.
14. Symons M, Derry JM, Karlak B, Jiang S, Lemahieu V, Mccormick F, Francke U, Abo A. Wiskott-Aldrich syndrome protein, a novel effector for the GTPase CDC42Hs, is implicated in actin polymerization. Cell 1996;84(5):723–734.
15. Nobes CD, Hall A. Rho, rac, and cdc42 GTPases regulate the assembly of multimolecular focal complexes associated with actin stress fibers, lamellipodia, and filopodia. Cell 1995;81(1): 53–62.
16. Machesky LM, Hall A. Rho: a connection between membrane receptor signaling and the cytoskeleton. Trends Cell Biol 1996; 6:304–310.
17. Zamir E, Geiger B. Molecular complexity and dynamics of cell-matrix adhesions. J Cell Sci 2001;114:3583–3590.
18. Ren XD, Kiosses WB, Schwartz MA. Regulation of the small GTP-binding protein Rho by cell adhesion and the cytoskeleton. EMBO J 1999;18(3):578–585.
19. Paddock SW, Dunn GA. Analysing collisions between fibroblasts and fibrosarcoma cells: fibrosarcoma cells show an active invasionary response. J Cell Sci 1986;81:163–187.
20. Nishimura KY, Isseroff RR, Nuccitelli R. Human keratinocytes migrate to the negative pole in direct current electric fields comparable to those measured in mammalian wounds. J Cell Sci 1996;109:199–207.
21. Boudreau N, Bissell MJ. Extracellular matrix signaling: integration of form and function in normal and malignant cells. Curr Opin Cell Biol 1998;10:540–646.
22. Gumbiner BM. Cell adhesion: the molecular basis of tissue architecture and morphogenesis. Cell 1996;84:345–357.
23. Settleman J. Getting in shape with Rho. Nat Cell Biol 2000;2: E7–E9.
24. Small JV, Kaverina I, Krylyshkina O, Rottner K. Cytoskeleton cross-talk during cell motility. FEBS Lett 1999;452:96–99.
25. Kaverina I, Krylyshkina O, Small JV. Regulation of substrate adhesion dynamics during cell motility. Int J Biochem Cell Biol 2002;34:746–761.
26. McClay KB, Grainger DW. Rho-A–induced changes in fibroblasts cultured on organic monolayers. Biomaterials 1999;20: 2435–2446.
27. Koenig AL, Gambillava V, Grainger DW. Correlating fibronectin adsorption with endothelial cell adhesion and signaling on polymer substrates. J Biomed Mater Res 2002;64A:20–37.
28. Putnam AJ, Cunningham JJ, Pillemer BB, Mooney DJ. External mechanical strain regulates membrane targeting of Rho GTPases by controlling the state of microtubule polymerization. Am J Physiol Cell Physiol 2003;284:C627–639.

Available online at www.sciencedirect.com
SCIENCE DIRECT
Biomaterials 26 (2005) 3105–3111
Biomaterials
www.elsevier.com/locate/biomaterials

Poly(*N*-isopropylacrylamide) (PNIPAM)-grafted gelatin hydrogel surfaces: interrelationship between microscopic structure and mechanical property of surface regions and cell adhesiveness

Shoji Ohya[a,*], Satoru Kidoaki[b], Takehisa Matsuda[b]

[a]*Department of Bioengineering, National Cardiovascular Center Research Institute, 5-7-1 Fujishirodai, Suita, Osaka 565-8565, Japan*
[b]*Division of Biomedical Engineering, Graduate School of Medicine, Kyushu University, 3-1-1 Maidashi Higashi-ku, Fukuoka 812-8582, Japan*

Received 24 May 2004; accepted 23 August 2004
Available online 30 September 2004

Abstract

Poly(*N*-isopropylacrylamide)-grafted gelatin (PNIPAM-gelatin) serves as a temperature-induced scaffold at physiological temperature. This study was aimed at determining the effect of the graft architecture of thermoresponsive PNIPAM-gelatin on the surface topography and elastic modulus of the hydrogels prepared with different architectured PNIPAM-gelatins: the surface topography and elastic modulus were determined by atomic force microscopy (AFM). PNIPAM-gelatin surfaces showed an irregularly concavo-convex structure with a vertical interval of approximately 1 μm regardless of the weight ratio of PNIPAM to gelatin (P/G: 5.8, 12, and 18). The elastic moduli of hydrogels varied at measured sites. The mean elastic moduli of PNIPAM-gelatin with the lowest P/G were low, but increased with increasing P/G. Human umbilical vein endothelial cells adhered and spread on PNIPAM-gelatin hydrogels with the highest P/G, whereas reduced adhesion and nonspreading, round-shaped cells resided on the hydrogels with lower P/Gs. Interrelationship between elastic modulus and cell adhesion and spreading potentials were discussed from physicochemical and cellular biomechanical viewpoints.
© 2004 Elsevier Ltd. All rights reserved.

Keywords: Poly(*N*-isopropylacrylamide)-grafted gelatin; Atomic force microscopy; Microscopic structure; Mechanical property; Cell adhesiveness

1. Introduction

Tissue engineering has recently been proposed as a promising therapeutic discipline for repairing or to replace diseased or lost tissues; moreover, some engineered tissues have been used for clinical applications [1–4]. Such tissues are fabricated ex vivo or in vivo with or without using synthetic or biologically derived macromolecules so as to provide an appropriate extracellular milieu. To reconstruct a functional tissue, the micro-extracellular environment for incorporated cells is essential. The extracellular space should be incorporated with a cell adhesion matrix and/or structural platform, and interconnected (microscopic) voids in order to facilitate a supply of oxygen and nutrients to cells, cell migration and tissue ingrowth.

We recently prepared a thermoresponsive artificial extracellular matrix (ECM), poly(*N*-isopropylacrylamide)-grafted gelatin (PNIPAM-gelatin) [5–8], which is prepared by quasi-living radical graft polymerization initiated from a gelatin molecule [9,10], and evaluated how the viability and proliferation of cells entrapped in a three-dimensional (3D) hydrogel depended on the graft architecture, including graft chain density and graft chain length of PNIPAM-gelatin [8]. As a rough approximation, bovine smooth muscle cells proliferated well in hydrogels prepared using PNIPAM-gelatin with a high weight ratio of PNIPAM to gelatin (P/G).

In this study, we investigated how cell adhesion on a hydrogel surface is influenced by the graft architecture

*Corresponding author. Tel.: +81-6-6833-5012; fax: +81-6-6872-8090.
E-mail address: ohya@ri.ncvc.go.jp (S. Ohya).

0142-9612/$ - see front matter © 2004 Elsevier Ltd. All rights reserved.
doi:10.1016/j.biomaterials.2004.08.006

of PNIPAM-gelatin. The effects of surface topography and surface mechanical strength, both of which are determined by atomic force microscopy (AFM), on cell adhesion and spreading potentials were evaluated and discussed from the physicochemical and biomechanical viewpoint.

2. Materials and methods

2.1. Materials

1-Ethyl-3-(3-dimethylaminopropyl) carbodiimide hydrochloride (WSC) was obtained from Dojindo Laboratories (Kumamoto, Japan). *N*-isopropylacrylamide (NIPAM) and 4-chloromethyl benzoic acid were obtained from Tokyo Chemical Industry Ltd. (Tokyo, Japan). NIPAM was used after recrystallization using a toluene–hexane solution. Gelatin (molecular weight: approximately 9.5×10^4 g/mol, from bovine bone) and sodium *N*,*N*-diethyldithiocarbamate trihydrate were obtained from Wako Pure Chemical Industry Ltd. (Osaka, Japan). Solvents and other reagents, all of which are of reagent grade, were purchased from Wako and used after conventional purification.

2.2. Preparation of PNIPAM-gelatin hydrogel

PNIPAM-gelatins with different graft densities (approximately 11, 23, and 34 graft chains per gelatin molecule; average molecular weight of the graft chain: approximately 5.0×10^4 g/mol) were prepared according to the procedure described previously [5–8]. Briefly, the amino groups of gelatin were reacted with the carboxyl group of 4-dithiocarbamylmethyl benzoic acid using the condensation reagent, WSC. The degree of dithiocarbamylation was adjusted with reaction time. Subsequently, NIPAM was polymerized from dithiocarbamate-derivatized gelatin in water under UV irradiation for 10 min (400 W Hg lamp, AH400RP, UV, Saitama, Japan; light intensity at 250 nm: 4.0 mW/cm^2). By graft density, three different PNIPAM-gelatins were prepared (PNIPAM/gelatin weight ratios (P/G) = 5.8, 12, and 18). Hydrogels were prepared from PNIPAM-gelatins with different P/G at 5 and 20 w/v% of aqueous solution (Chemical structures are shown in Fig. 1). The aqueous or M199 solutions of PNIPAM-gelatins (concentration: 5 and 20 w/v%, 100 μL) placed on the tissue culture dish (diameter: 35 mm, Iwaki Glass, Tokyo, Japan) fixed on the stage of AFM equipment were warmed to 37 °C to form white opaque hydrogels. The water or M199 was added onto the hydrogel, which were subjected to surface topological and mechanical strength characterizations described below. The formed hydrogel tightly adhered on the bottom of the dish.

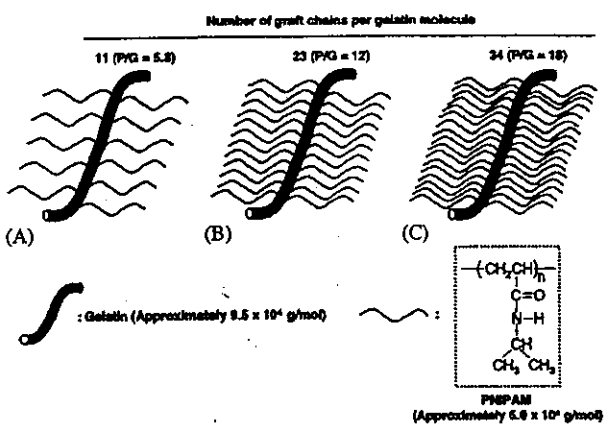

Fig. 1. Schematic structure of PNIPAM-gelatins with different graft chain densities.

2.3. Surface observation and elastic modulus

The surface images and force-versus-indentation (F–δ) curves of the hydrogels in water or M199 at 37 °C were measured by AFM (Nanoscope IIIa, Dimension 3000, Digital Instruments), using a commercial Si_3N_4 probe tip (manufacturing spring constant: 0.06 N/m (the value was used for the calculation of elastic modulus without further validation. Since the same tip was used throughout the study, the discussion was made on basis of the relative values); Digital Instruments, Santa Barbara, CA, USA). The probe tip was equipped with a commercial fluid cantilever folder (Digital Instruments), and immediately immersed into water or M199. The measurement was performed in water or M199 at 37 °C. To control sample temperature, AFM equipment was placed in a box maintained at 37 °C using heater with a thermocontroler (Nikon, Japan). Surface images (Scanning size: 10 μm × 10 μm) were obtained by a tapping mode (resonance frequency: 7.0 kHz).

F–δ curves were measured linearly every 100 nm (total of 101 points measured) by a contact mode. Elastic moduli were calculated from the F–δ curves according to the Hertz model described below [11]. If the tip is infinitely stiff and conical in shape, the Hertz model predicts

$$F = \frac{2\tan\alpha}{\pi}\frac{E}{1-\upsilon^2}\delta^2, \quad (1)$$

where F is the loading force, E is the elastic modulus, υ is the Poisson ratio, α is the open angle of the tip, and δ is the indentation depth. Here, open angle α was 35° and Poisson ratio υ was fixed to 0.5 for simplification. Therefore, elastic moduli were calculated from F–δ curves fitted to the equation using a linear least-squares method.

2.4. Cell adhesiveness on PNIPAM-gelatin hydrogels

Human umbilical vein endothelial cells (HUVECs) were stained with a fluorescent dye of benzoxazolium, 3-octadecyl-2-[3-(3-octadecyl-2(3H)-benzoxazolylidene)-1-propenyl]-, perchlorate (DiO, Molecular Probes Inc., Eugene, USA), before use. M199 solutions (70 μL) of PNIPAM-gelatin (P/G = 5.8, 12, and 18, concentration; 5 w/v% or 20 w/v%) were placed on the surface enclosed with a stainless-steel ring ($\varnothing = 15$ mm) placed in the tissue culture dish at room temperature. The dish was placed in humidified 5% CO_2 incubator for 30 min to form a white opaque hydrogel. An M199 (10% FCS, 0.5 mL) suspension of HUVECs (cell density: 2.0×10^4 cells/mL) was poured onto the hydrogel maintained at 37 °C. After 2 days of incubation, cell morphology was observed by confocal laser scanning microscopy (Radiance 2000, Biorad, CA, USA) (wavelength: 488 nm (excitation) and 510 nm (fluorescence)).

3. Results

Hydrogels were prepared by thermal phase inversion using three PNIPAM-gelatins with different graft chain densities (Figs. 1A–C). These PNIPAM-gelatins have approximately 11, 23, and 34 graft chains per gelatin molecule but have a fixed average molecular weight of the graft chain (approximately 5.0×10^4 g/mol). The weight ratios (P/G) of the grafted chain (PNIPAM) to the main chain (gelatin) of these three PNIPAM-gelatins were 5.8, 12, and 18 in accordance with the graft chain density. The concentrations of PNIPAM-gelatins in hydrogels thus prepared were 5 and 20 w/v% of water and M199 culture medium. These hydrogels were adhered on the bottom of the dishes. Surface topography and surface micro-mechanical strength were determined by AFM. Cell adhesion and spreading of fluorescently labeled HUVECs on these hydrogel surfaces were determined by confocal laser scanning microscopy.

3.1. Microscopic topography of hydrogels

AFM images obtained in water or M199 show that all the surfaces of PNIPAM-gelatin hydrogels have microscopic concavo-convex structure as clearly injected by scattered dark or bright images, which may contain micropores and pits, regardless of P/G, PNIPAM-gelatin concentration, or solution (Fig. 2: upper). Fig. 2 (lower) shows the surface topographic images of these hydrogels of transversely scanned 10-μm-wide regions (dotted line in the upper figure). Increasing P/G appears to result in a more roughened topography with finer tiny pits (Figs. 2A–C). Several tiny pits with a depth of approximately half micrometer appeared in the scanned width of 10 μm. Little significant topographic difference was observed between those in water and in M199 (Figs. 2C and D). Reducing the concentration from 20 to 5 w/v% resulted in the disappearance of the tiny pits (Fig. 2E).

3.2. Elastic modulus of hydrogels

The micromechanical properties of more than 100 surface regions for each sample were determined by the force indentation (F–δ) technique. All the F–δ curves determined from the hydrogel surfaces along the dotted lines shown in Fig. 2 (upper) by the indentation of an AFM probe tip were parabolic (Fig. 3). Since a linear

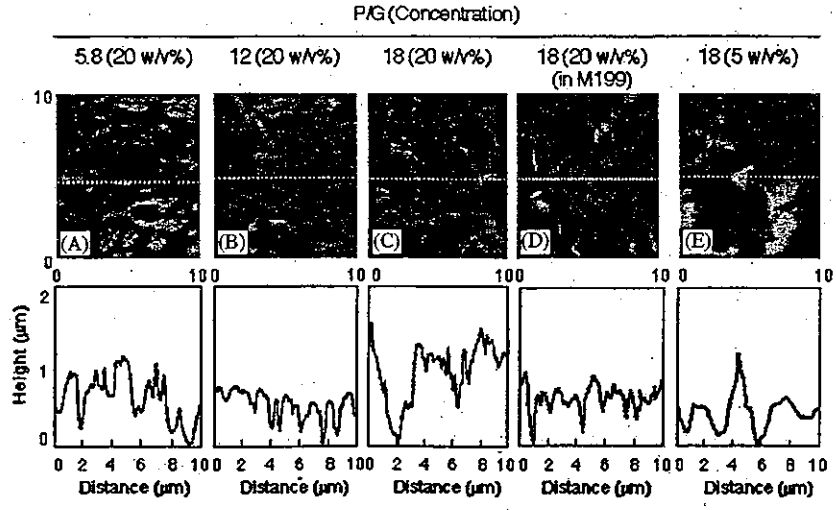

Fig. 2. Microscopic observation of PNIPAM-gelatin hydrogel surface by AFM in water (A)(B)(C)(E) and in M199 (D). Weight ratio of PNIPAM to gelatin (P/G): 5.8 for (A), 12 for (B), 18 for (C), (D) and (E). Hydrogel concentration: 20 w/v% for (A)(B)(C)(D), 5 w/v% for (E). Dark and bright areas are concave and convex areas, respectively.

relationship between F and δ^2 is held (Fig. 3B), the conical Hertz model was applied to calculate elastic moduli. Fig. 4 shows the relationship between the calculated elastic modulus and the height of the measured point for three hydrogels prepared at 20 w/v%, which was obtained from 101 points on each white-dotted line in Fig. 2 (the height is defined as the distance from the lowest or bottom line in the topography shown in Fig. 2: lower). The general tendency is that the elastic moduli appear to increase with increasing P/G, although the values of the determined elastic moduli were scattered. A majority of the elastic moduli of hydrogels with PNIPAM-gelatins of P/G of 5.8 were below 100 kPa, the average elastic modulus was 53 ± 21 kPa, and the height was less than 1 μm (Table 1 and Fig. 4). For hydrogels with PNIPAM-gelatin of P/G of 12, the population of elastic moduli higher than 100 kPa (around 20%) was increased. For hydrogels with P/G of 18, most of the moduli (more than 80%) were over 100 kPa irrespective of solutions. The average elastic moduli in water and M199 were 222 ± 64 and 244 ± 89 kPa, respectively. There is little significant difference in surface mechanical strength between hydrogels in water and in M199. These results indicate that highly aggregated PNIPAM were distributed on the hydrogel surface made of PNIPAM-gelatin with a high P/G of 18. At lower concentration (5 w/v%), the population of elastic moduli higher than 150 kPa decreased to 5% of the total population (data not shown). These indicate that a higher P/G and higher concentration result in a higher degree of aggregation and a higher surface distribution.

It is interesting to see how the elastic modulus of the hydrogel correlates with the surface topography (height). The calculated correlation coefficients are shown in Table 1. The correlation coefficients between surface topography and elastic modulus on PNIPAM-gelatin hydrogels with the lowest P/G of 5.8 were 0.3, whereas that of hydrogel with P/G of 18 was 0.45, implying that convex sites are stiffer than concave sites.

3.3. Cell adhesiveness on hydrogels

Confocal laser scanning microscopic images demonstrated the adhesion and spreading states of fluorescently labeled HUVECs on PNIPAM-gelatin hydrogels after two days of incubation (Fig. 5). Cells adhered and spread on hydrogels with higher P/Gs (12 and 18), but few cells adhered on that with P/G of 5.8. The number of spreading cells qualitatively appeared to increase with increasing P/G. At P/G of 18, there is a small difference between the spreading states of cells in 5 w/v% and 20 w/v% hydrogels.

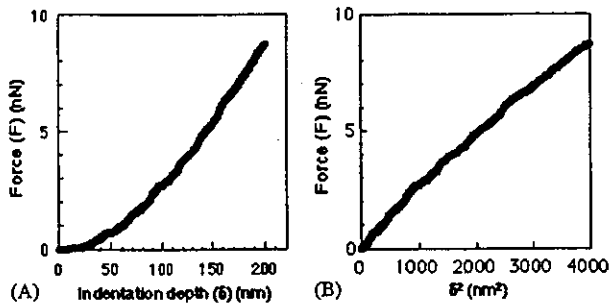

Fig. 3. (A) Force–indentation curve (F–δ curve) on PNIPAM-gelatin hydrogel by AFM. (B) F–δ^2 plots for analysis with Hertz model. Linear F–δ^2 using conical tip assumption.

4. Discussion

Cell adhesion, spreading and proliferation proceed via multiparameter-driven processes. Apart from biological factors (such as adhesion proteins and growth factors) and external mechanical-stress field (hydrodynamic and compressive forces), the substrate is a major determinant, which involves chemical compositions, mechanical properties and topography at the outer-surface region of the substrate. Almost three decades ago, Maroudas hypothesized that the rigidity or stiffness of the

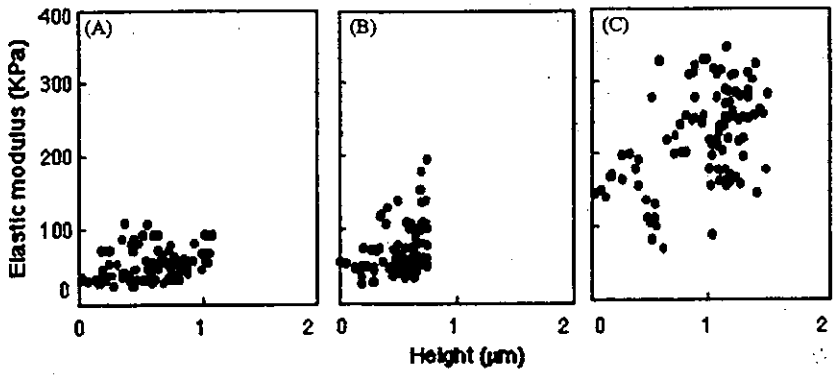

Fig. 4. Interrelationship between surface topography and elastic modulus evaluated from F–δ curves. The weight ratio of PNIPAM to gelatin (P/G): 5.8 for (A), 12 for (B), 18 for (C). Concentration (20 w/v%).

Table 1
Physical properties of PNIPAM-gelatin hydrogel

Hydrogel no.	PNIPAM-gelatin		Concentration (w/v%) (solution)	Elastic modulus (kPa)	Correlation coefficient[c]
	Graft density[a]	P/G[b]			
1	11	5.8	20 (water)	53±21	0.30
2	23	12	20 (water)	70±34	0.34
3	34	18	20 (water)	222±64	0.45
4	34	18	20 (M199)	244±89	ND[d]
5	34	18	5 (water)	52±36	ND[d]

[a]Number of graft chains per gelatin molecule.
[b]Weight ratio of PNIPAM to gelatin.
[c]Correlation coefficient between surface height and elastic modulus. Molecular weight of graft chain; approximately 5.0×10^4 g/mol (determined by GPC using PEG standards).
[d]ND; not determined. Number of measured points for each run were 101.

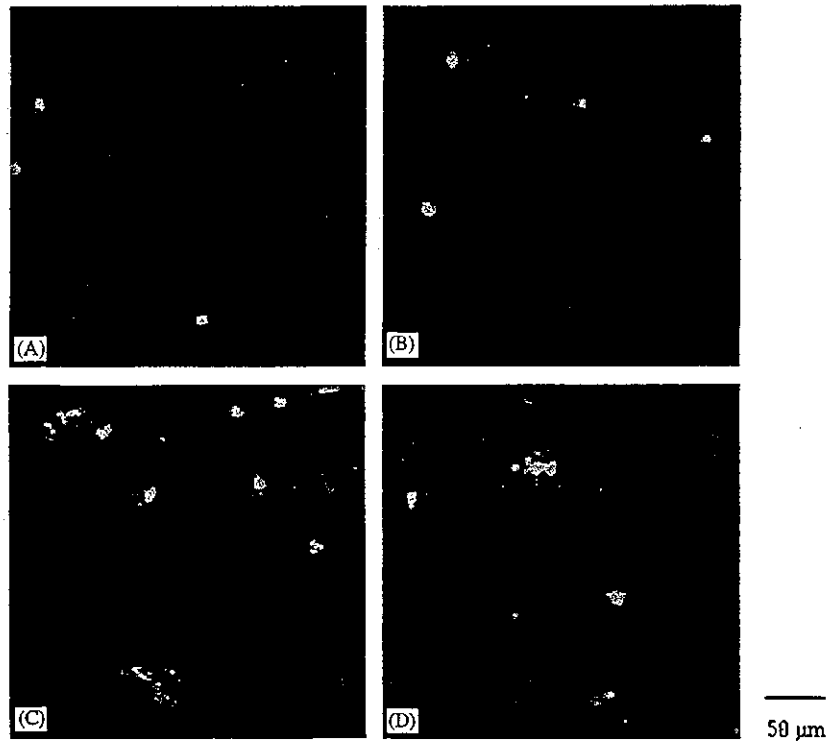

Fig. 5. Confocal laser scanning microscopic observation of HUVECs on PNIPAM-gelatin hydrogels. P/G: 5.8 for (A), 12 for (B), 18 for (C) and (D). Hydrogel concentration: 20 w/v% for (A)(B)(C), 5 w/v% for (D). HUVECs adhered and spread on hydrogels with P/G of more than 12. Cell morphology was dependent on P/G, not on the concentration of PNIPAM-gelatin.

substrate surface determines cell adhesiveness and the state of spreading. Such cell adhesiveness and spreading are enhanced by the rigidity of the substrate. Maroudas also postulated that cells require a rigid scaffolding to withstand tension exerted by spreading [12]. Using a deformable silicone thin film, Harris et al. showed that cell adhesion/spreading is strongly governed by surface rigidity/deformability [13]. Recently, Pelham and Wang demonstrated that cell focal adhesion and locomotion on flexibility-varied acrylamide gels are regulated by hydrogel substrate flexibility [14] and suggested the possible involvement of tyrosine phosphorylation, which is activated by local tension at adhesion sites [15,16]. Thus, many studies have implicated that mechanotransduction across the adhesion site between cell focal adhesion plaques and the extracellular matrix attached to the substrate determines cellular fundamental behaviors including adhesion, spreading, migration, proliferation, differentiation, re-differentiation, metastasis, and apoptosis.

The extracellular space design, which determines biological conditions suitable for cellular activities, is one of the most important factors in the fabrication of functional vital engineered tissues. Various design criteria have to be considered from the microscopic to the macroscopic level. The microenvironment on the hydrogel must determine the cell adhesiveness. In this study, we attempted to define the interrelationship between the microscopic surface structural and mechanical properties and cell adhesiveness of PNIPAM-gelatin hydrogel surfaces. Hydrogel surfaces, prepared by warming PNIPAM-gelatin aqueous and M199 solutions at 37 °C, were observed by AFM. All surfaces of PNIPAM-gelatin hydrogels have a nano-ordered concavo-convex structure over the scanning area, regardless of P/G (Fig. 2). The general tendency was that the hydrogel prepared using PNIPAM-gelatin with the highest P/G exhibited the most roughened surface topography (Fig. 2: C). It is suggested that the hydrogel contains interconnected micropores or voids, through which nutrients and oxygen can diffuse into the interior of the hydrogel.

On the other hand, the relationship between force (F) and indentation depth (δ) on the hydrogels fitted well to the conical Hertz model (linear relationship between F and δ^2; Fig. 3B) by which the elastic modulus was calculated. To validate how the measured elastic modulus is correct, we determined the elastic modulus (70 ± 11 kPa) of an agarose gel (3 w/v%) as standard sample. The obtained value reasonably agrees with the previously reported elastic modulus of 90 kPa [17,18]. As shown in Fig. 4, the calculated elastic moduli of PNIPAM-gelatin hydrogels increased with increasing P/G, although the measured values were scattered. It is speculated that the hydrogels must consist of roughly two domains in the continuous phase of water: One domain is a highly hydrated gelatin (soft) domain and the other is an aggregated PNIPAM (rigid) domain, which were formed by the intra- and inter-molecular associations of dehydrated PNIPAM graft chains, respectively. Our recent study showed that confocal laser scanning microscopic observation with reflection mode clearly demonstrated that hydrophobically clustered PNIPAM were scattered in the interior of the hydrogel [8]. For the hydrogel with P/G of 5.8, the major measured values were low, suggesting that the measured sites are associated with small-sized loosely aggregated PNIPAM domains. With an increase in P/G to more than 12, the obtained values became larger, indicating that the measured sites are associated with larger-sized, highly aggregated domains, the population and size of which must be increased with an increase in P/G.

The fine-structure and physical properties of hydrogel may change between water and culture medium due to containing many compounds such as salts and amino acids in culture medium. To examine the effect of the conditions, surface microtopography and elastic modulus measurement of hydrogel with P/G of 18 were conducted in cell culture medium of M199. The topography and elastic modulus were found to be similar to those in water (Table 1).

On the other hand, the correlation coefficients between the heights and elastic moduli of hydrogel surfaces were positive but not large (Table 1). However, an increased correlation coefficient with an increase in P/G was observed. Taken together with these lines of experimental evidence, it can be considered that most of convex region must be rigid, and concavo region must be soft (Fig. 4).

Cell adhesiveness was enhanced by increasing P/G (Fig. 5). A high P/G caused strong aggregation among PNIPAM chains, so that the higher strength of the hydrogel results in an enhanced higher capability of withstanding cell traction force, resulting in cell spreading. Thus, an appropriate balance of surface micromechanical strength derived from dehydrated PNIPAM aggregates and water-swollen cell-adhesive gelatin molecule provides cell adhesive and spreading environment on hydrogels. Scattered stiff regions probably derived from hydrophobically clustered PNIPAM may act as cell adhesion anchors which withstand against the cell traction strength.

5. Conclusion

Thermoresponsive hydrogels prepared using PNIPAM-gelatins with different architecture exhibited surfaces with concavo-convex structure, roughened surface topography and variable elastic modulus, both of which were determined by AFM. HUVECs adhered and spread well on the hydrogel prepared using PNIPAM-gelatin with a high P/G. These results show that surface elastic modulus can be a determinant of cellular behavior on hydrogels.

Acknowledgement

This study was financially supported by Ministry of Education, Culture, Sports, Science and Technology under Grant No. 14780665 and No. 15200038. One of the authors (S.O.) appreciates Dr. Y. Nakayama for technical advises.

Reference

[1] Bell E. Strategy for the selection of scaffolds for tissue engineering. Tissue Engineering 1995;1:163–79.
[2] Hutmacher DW, Goh JC, Teoh SH. An introduction to biodegradable materials for tissue engineering applications. Ann Acad Med Singapore 2001;30:183–91.

[3] Drury JL, Mooney DJ. Hydrogels for tissue engineering: scaffold design variables and applications. Biomaterials 2003;24:4337–51.
[4] Freed LE, Vunjak-Novakovic G, Biron RJ, Eagles DB, Lesnoy DC, Barlow SK, Langer R. Biodegradable polymer scaffolds for tissue engineering. Bio/Technology 1994;12:689–93.
[5] Morikawa N, Matsuda T. Thermoresponsive artificial extracellular matrix: *N*-isopropylacrylamide-graft-copolymerized gelatin. J Biomater Sci Polym Ed 2002;13:167–83.
[6] Matsuda T. Molecular design of functional artificial extracellular matrix: thermoresponsive gelatin. Jpn J Artif Organs 1999; 28:242–5.
[7] Ohya S, Nakayama Y, Matsuda T. Material design for artificial extracellular matrix: cell entrapment in poly(*N*-isopropylacrylamide) (PNIPAM)-grafted gelatin hydrogel. J Artif Organs 2001;4:308–14.
[8] Ohya S, Matsuda T. Poly(*N*-isopropylacrylamide) (PNIPAM)-grafted gelatin as thermoresponsive three-dimensional artificial extracellular matrix: molecular and formulation parameters vs. cell proliferation potential. Submitted for publication.
[9] Otsu T, Yoshida M, Tazaki T. A model for living radical polymerization. Makromol Chem Rapid Commun 1982;3:133–40.
[10] Nakayama Y, Matsuda T. Surface macromolecular architectural designs using photo-graft copolymerization based on photochemistry of benzyl *N*,*N*-diethyldithiocarbamate. Macromolecules 1996;29:8622–30.
[11] Weisenhorn AL, Khorsandi M, Kasas S, Gotzos V, Butt HJ. Deformation and height anomaly of soft surfaces studied with an AFM. Nanotechnology 1993;4:106–13.
[12] Maroudas NG. Chemical and mechanical requirements for fibroblast adhesion. Nature 1973;244:363–4.
[13] Harris AK, Wild P, Stopak D. Silicone rubber substrata: a new wrinkle in the study of cell locomotion. Science 1980;208:177–9.
[14] Pelham RJ, Wang YL. Cell locomotion and focal adhesions are regulated by substrate flexibility. Proc Natl Acad Sci USA 1997;94:13661–5.
[15] Zamir E, Katz M, Posen Y, Erez N, Yamada KM, Katz BZ, Lin S, Lin DC, Bershadsky A, Kam Z, Geiger B. Dynamics and segregation of cell-matrix adhesions in cultured fibroblasts. Nat Cell Biol 2000;2:191–6.
[16] Katz BZ, Zamir E, Bershadsky A, Kam Z, Yamada KM, Geiger B. Physical state of the extracellular matrix regulates the structure and molecular composition of cell-matrix adhesions. Mol Biol Cell 2000;11:1047–60.
[17] Nitta T, Haga H, Kawabata K, Abe K, Sambongi T. Comparing microscopic with macroscopic elastic properties of polymer gel. Ultramicroscopy 2000;82:223–6.
[18] Haga H, Sasaki S, Morimoto M, Kawabata K, Ito E, Abe K, Sambongi T. Imaging elastic properties of soft materials immersed in water using force modulation mode in atomic force microscopy. Jpn J Appl Phys 1998;37:3860–3.

Available online at www.sciencedirect.com
SCIENCE DIRECT®
Biomaterials 26 (2005) 655–659
Biomaterials
www.elsevier.com/locate/biomaterials

Technical note

The potential of poly(*N*-isopropylacrylamide) (PNIPAM)-grafted hyaluronan and PNIPAM-grafted gelatin in the control of post-surgical tissue adhesions

Shoji Ohya[a,*], Hiromichi Sonoda[a,b], Yasuhide Nakayama[a], Takehisa Matsuda[b]

[a] *Department of Bioengineering, National Cardiovascular Center Research Institute, 5-7-1 Fujishirodai, Suita, Osaka 565-8565, Japan*
[b] *Division of Biomedical Engineering, Graduate School of Medicine, Kyushu University, 3-1-1 Maidashi, Higashi-ku, Fukuoka 812-8582, Japan*

Received 12 February 2004; accepted 13 March 2004

Abstract

Poly(*N*-isopropylacrylamide)-grafted hyaluronan (PNIPAM–HA) and PNIPAM-grafted gelatin (PNIPAM–gelatin), which exhibit sol-to-gel transformation at physiological temperature, were applied as control of tissue adhesions: tissue adhesion prevention material and hemostatic aid, respectively. The rat cecum, which was abraded using surgical gauze, was coated with PNIPAM–HA-containing PBS (concentration: 0.5 w/v%). The coated solution was immediately converted to an opaque precipitate at body temperature, which weakly adhered to and covered the injured rat cecum. One week after coating, tissue adhesion between the PNIPAM–HA-treated cecum and adjacent tissues was significantly reduced as compared with that between non-treated tissue and adjacent tissues. On the other hand, the coating of bleeding spots of a canine liver with PNIPAM–gelatin-containing PBS (concentration: 20 w/v%) resulted in spontaneous gel formation on the tissues and subsequently suppressed bleeding. Although these thermoresponsive tissue adhesion prevention and hemostatic materials are still prototypes at this time, both thermoresponsive biomacromolecules bioconjugated with PNIPAM, PNIPAM–HA and PNIPAM–gelatin, may serve as a tissue adhesion prevention material and hemostatic aid, respectively.
© 2004 Elsevier Ltd. All rights reserved.

Keywords: Poly(*N*-isopropylacrylamide)-grafted biomacromolecules; Gel; Thermoresponsiveness; Tissue adhesion prevention; Hemostasis

1. Introduction

The prompt management of normal wound healing during and after surgical treatment may predict the post-surgical healing of tissues. Hemostatic control during surgical operation and tissue adhesion prevention after surgery are two critical issues in wound healing. To this end, various approaches and materials have been developed and tested over the years. However, "ideal" wound-healing materials have not been realized as yet.

Post-surgical tissue adhesion, which results from malignant healing response of a damaged tissue to a non-injured tissue, often causes life-threatening complications or necessitates re-operation. To reduce tissue adhesion, the use of physical barrier membranes to separate adjacent tissues during the healing process has been proposed and examined [1]. Carboxymethylcellulose [1,2], dextran [3] and oxidized regenerated cellulose [1–4] films have been clinically used as such membranes with some therapeutic effects. Hyaluronan (HA), which is an extracellular matrix component, is known to temporarily prevent tissue adhesion [5] when such a solution is coated on damaged tissue. However, HA is rapidly biodegraded by hyaluronidase and removed away from the injury sites [6].

On the other hand, tissue adhesive glue or hemostatic aids have been used when bleeding cannot be controlled during surgery. Fibrin glue has been clinically used in these cases. However, its major drawbacks are its low mechanical strength and potential infection risk inherent to blood origin. Semisynthetic and synthetic materials such as cyanoacrylate derivatives [7,8], gelatin–resorcinol–formaldehyde [8], and fluorinated hexamethylene diisocyanate-based urethane prepolymers [9] have been applied as surgical adhesives. Although they have

*Corresponding author. Tel.: +81-6-6833-5012; fax: +81-6-6872-8090.
E-mail address: ohya@ri.ncvc.go.jp (S. Ohya).

0142-9612/$ - see front matter © 2004 Elsevier Ltd. All rights reserved.
doi:10.1016/j.biomaterials.2004.03.002

appropriate tissue adhesiveness, cytotoxicity and severe inflammatory reactions with the use of the former two glues and very slow degradation with the last glue are the major drawbacks, respectively.

Regardless of tissue adhesion prevention or hemostatic aids, rapid sol-to-gel formation is necessary to cover the injured or bleeding sites of a tissue. Such a phase transition is desired to occur within a few minutes after application at physiological temperature. We previously prepared poly(*N*-isopropylacrylamide) (PNIPAM)-grafted hyaluronan (PNIPAM–HA) [10,11] and PNIPAM-grafted gelatin (PNIPAM–gelatin) [12–14]. These were soluble in water at room temperature but precipitated or gelled at physiological temperature due to thermoresponsive phase transition characteristics of PNIPAM. In this study, we explored the potential applicability of thermoresponsive PNIPAM–HA and PNIPAM–gelatin as a tissue adhesion prevention material or hemostatic aid, respectively.

2. Materials and methods

2.1. Material

Sodium hyaluronate (HANa, molecular weight: ca. 5.0×10^5 g/mol) was supplied by Seikagaku Kogyo Co. Ltd., Gelatin (molecular weight: ca. 9.5×10^4 g/mol, from bovine bone) and the solvents, which were of special reagent grade, were purchased from Wako Pure Chemical Industry Ltd., (Osaka, Japan) and used after conventional purification.

2.2. Cell adhesion on PNIPAM–HA film

An aqueous solution of PNIPAM–HA (concentration: 0.5 w/v%) was coated onto a circular cover glass (diameter: 14.5 mm, Matsunami Glass Co. Ltd., Osaka, Japan) and dried at room temperature. Rat fibroblasts at a density of 2.0×10^4 cells/ml were seeded on PNIPAM–HA films. After 3 h of incubation, cell morphology was observed by phase-contrast microscopy (Diaphoto, Nikon, Tokyo, Japan). All the procedures including cell culture were carried out at 37°C.

2.3. Tissue adhesion prevention efficacy of PNIPAM–HA

Tissue adhesion prevention efficacy was assessed using a rat cecum abrasion model [1,4]. Anesthesized Wistar rats were subjected to laparotomy. Each rat cecum was abraded with a surgical gauze. A PBS (0.5 ml) of PNIPAM–HA (concentration: 0.5 w/v%) was coated onto the cecum. One week after application, the incidence and severity of adhesions of the cecum to adjacent tissues were evaluated according to the following system: after harvesting the cecum and fixing it in formalin neutral buffer solution (pH 7.4, Wako Pure Chemical Industry Ltd., Osaka, Japan) at 37°C, the specimens stained with hematoxylin–eosin (H&E) and Masson's trichrome were observed by light microscopy (VANOX-S, Olympus, Tokyo, Japan).

0: No cecum adhesions
1: Firm adhesion with easily dissectable plane
2: Adhesion with dissectable plane causing mild tissue trauma
3: Fibrous adhesion with difficult tissue dissection
4: Fibrous adhesion with non-dissectable tissue planes.

2.4. Histological analysis of tissue adhesion prevention efficacy for PNIPAM–HA precipitate

For histological analysis, PNIPAM–HA-treated rat ceca, after seven days, were fixed with 10% formalin neutral buffer solution (pH 7.4) for more than seven days, dehydrated in a graded ethanol series, embedded in paraffin, and sectioned at 5 μm thickness. After staining with H&E or Masson's trichrome, the specimens were evaluated by light microscopy.

2.5. Hemostatic characteristics of PNIPAM–gelatin

The hemostatic characteristics of PNIPAM–gelatin were evaluated using a canine liver model (weight: 25 kg) and a Wistar rat aorta model (average weight: 250 g). The canine liver was abraded with trephine in laparotomy and the rat aorta was clamped and punctured using a 23-gage needle. A PBS of PNIPAM–gelatin (concentration: 20 w/v%) was coated on the bleeding spot. The efficacy of hemostasis was determined by gross observation.

3. Results

3.1. PNIPAM–HA

When rat fibroblasts were seeded and cultured on PNIPAM–HA film, cast from their aqueous solution, a markedly reduced adhesion and suppressed spreading (mostly round shape) were observed (Fig. 1), indicating that PNIPAM–HA is a non-cell-adhesive matrix.

The efficacy of the PNIPAM–HA film for tissue adhesion prevention was evaluated using a rat cecum abrasion model [1,4]. When a PBS solution of PNIPAM–HA was coated on a rat cecum, an opaque PNIPAM–HA precipitate was immediately formed around the cecum at body temperature. One week after coating, ceca without PNIPAM–HA coating strongly adhered to adjacent tissues (Figs. 2 and 3). When the adhesion incidence of each rat was scored according to the scoring

rate described in Section 2, the average overall score (4: severe adhesion, 0: non-adhesion) was 2.2 ± 0.7 ($n = 9$) and the experimental sample number over score 2, which shows tissue adhesion, was counted as eight out of nine rats examined (Table 1). On the other hand, the reduced adhesion of the cecum to adjacent tissues was observed, although the PNIPAM–HA-treated ceca weakly adhered to adjacent tissues (Figs. 2 and 3). The average overall score was 1.3 ± 0.5 ($n = 8$). The experimental sample number over score 2 was two out of eight rats examined (Fig. 2 and Table 1). These results indicate that the in situ formed PNIPAM–HA precipitate significantly reduced the degree of adhesion and occurrence of tissue adhesion of the rat cecum to adjacent tissues.

3.2. PNIPAM–gelatin

A PBS solution of PNIPAM–gelatin (20 w/v%) was coated on the bleeding spots generated by pricking a canine liver and a rat aorta with a needle. The solution was immediately converted to an elastic hydrogel on the

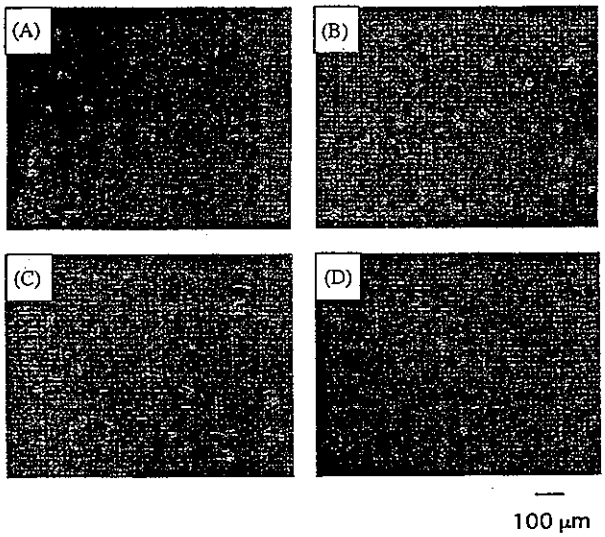

Fig. 1. Phase-contrast micrographs of rat fibroblasts (seeding density: 2.0×10^4 cells/ml) on glass (A)(C), PNIPAM–HA (B)(D) surfaces at 37°C immediately (A)(B) or after 3-h incubation (C)(D).

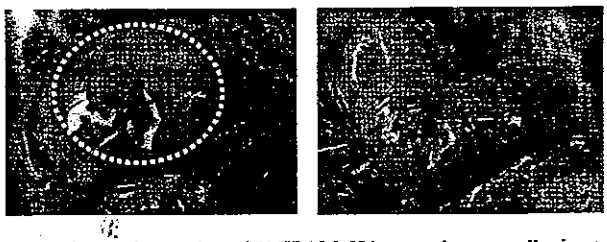

Fig. 2. Gross observation of PNIPAM–HA-treated cecum adhering to adjacent tissues one week after coating. Left: Non-PNIPAM–HA-treated cecum where omentum tissue adhered to and covered the injured cecum. Right: PNIPAM–HA-treated cecum without tissue adhesion.

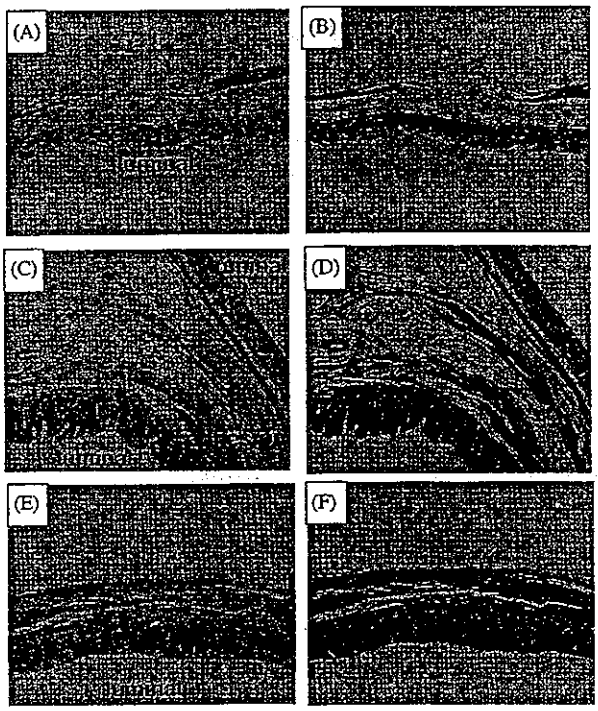

Fig. 3. Histological analysis of PNIPAM–HA-treated cecum adhering to adjacent tissues. Specimens were stained with H&E (A)(C)(E) and Masson's trichrome (B)(D)(F). PNIPAM–HA-treated cecum: (A) and (B), immediately after covering (E) and (F), 7 days after coating. Non-PNIPAM–HA-treated cecum: (C) and (D), 7 days after coating.

Table 1
Adhesion score of rat cecum

Sample	Adhesion score[a]	n	Ratio ⩾score 2
Non-treated	2.2 ± 0.7	9	8/9
PNIPAM-HA-treated	1.3 ± 0.5	8	2/8

[a] Adhesion scores are as follows: 0: No cecum adhesions, 1: Firmly adhesion with easily dissectable plane, 2: Adhesion with dissectable plane causing mild tissue trauma, 3: Fibrous adhesion with difficult tissue dissection, 4: Fibrous adhesion with nondissectable tissue planes.

bleeding spots (Fig. 4). The hydrogel weakly adhered to and covered the injured sites, resulting in hemostasis, which was completed within a minute after coating (Fig. 4). Pulsation was maintained, and no bleeding was observed within the experimental time observed (1–2 h after application).

4. Discussion

Fundamental requirements for "ideal" wound-healing materials are as follows: (1) viscous liquid form to

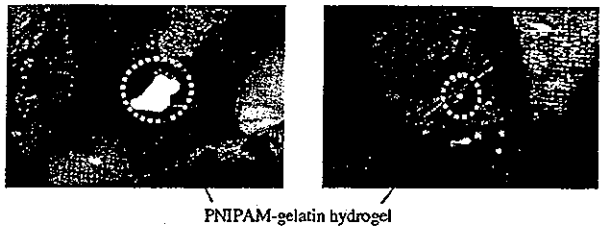

Fig. 4. Hemostases of bleeding from canine liver (left) and rat aorta (right) covered with PNIPAM–gelatin solution (20 w/v%). Spontaneous hydrogel formation and hemostases were observed. No re-bleeding was observed during 1-h after coating. Pulsatile-induced periodic dilation/contraction was observed on the dissected rat aorta.

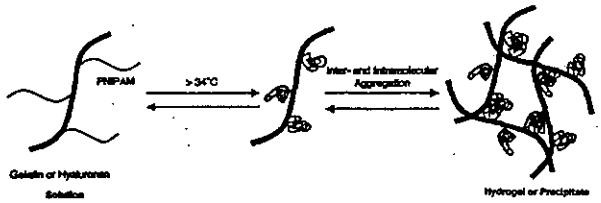

Fig. 5. Thermoresponsive gelation mechanism of PNIPAM–HA and PNIPAM–gelatin. Due to the dehydration of the hydrated amide group above lower critical solution temperature (LCST), PNIPAM graft chains were precipitated to form multimolecular aggregates. At high concentrations of PNIPAM-grafted biomacromolecules, the entire solution gelled to produce an opaque hydrogel and at low concentrations, a white precipitate was obtained.

completely cover complex-shaped tissue surfaces, (2) rapid formation of a swollen gel-like film or a precipitate when applied to injured tissues, (3) non-cell adhesiveness for tissue adhesion prevention and cell adhesiveness for hemostatic aids, and (4) appropriate biodegradability. That is, a wound-healing material should be biodegraded and sorpted with normal healing. Although various approaches and attempts have been carried out to meet the requirements listed above, in situ-applicable liquid-type materials, which include cyanoacrylate and fibrin glue, are limited (the major drawbacks associated with these hemostatic aids are described in Section 1) [7–9]. In this article, we applied thermoresponsive biomacromolecules (PNIPAM–HA and PNIPAM–gelatin) as wound-healing materials to meet the target requirements as listed above.

On a PNIPAM–HA film, cast from its aqueous solution at room temperature, the adhesion and spreading of fibroblasts were markedly inhibited (Fig. 1), which is due to the very highly swollen gel-like structure of HA (Fig. 5). When such a solution was applied to a rat cecum tissue, a slightly opaque precipitate was spontaneously formed. One week after application, markedly reduced adhesion of the PNIPAM–HA-treated cecum to adjacent tissues was observed while the non-treated cecum adhered to adjacent tissues, producing collagenous tissues (Fig. 3 and Table 1). Thus, in situ swollen precipitate of PNIPAM–HA effectively functioned in preventing tissue adhesion between the cecum and adjacent tissues.

As for thermoresponsive hemostatic aids, our previous study showed that PNIPAM–gelatin served as an artificial extracellular matrix material: the aqueous solution of PNIPAM–gelatin was immediately converted to a hydrogel, in which cells can adhere and proliferate. When PNIPAM–gelatin-containing PBS was coated on the bleeding sites of the canine liver and rat aorta, the solution was immediately converted to an opaque elastic hydrogel (Fig. 4). The hydrogel fully covered and weakly adhered to the bleeding sites, resulting in complete hemostasis on both tissues. The PNIPAM–gelatin-coated aorta pulsated well, indicating that the PNIPAM–gelatin formed quite elastic hydrogel and the hydrogel did not interfere with the periodic pulsation of a high-pressure circulatory system.

5. Conclusion

Although this article describes very limited experiments on tissue adhesion control using PNIPAM–HA and PNIPAM–gelatin, the bioconjugation of thermoresponsive synthetic materials and extracellular-matrix derived biomacromolecules, which thermally form precipitate or hydrogel, can provide a new prototype of wound-healing materials and promising procedures. Further studies to improve the properties required for both tissue adhesion and tissue adhesion prevention and to examine a longer term performances are needed. Such studies are ongoing in our laboratory.

Acknowledgements

The authors are grateful to Seikagaku Kogyo Co. Ltd., for the supply of sodium hyaluronate. This study was financially supported by Ministry of Education, Culture, Sports, Science and Technology under Grant No. 14780665 and No. 15200038.

References

[1] diZerega GS. Contemporary adhesion prevention. Feritl Steril 1994;61:219–35.
[2] Burns JW, Colt MJ, Burgess LS, Skinner KC. Preclinical evaluation of seprafilm™ bioresorbable membrane. Eur J Surg 1997;577(suppl.):40–8.
[3] Diamond MP, DeCherney AH, Linsky CB, Cunninghan T, Constantine B. Assesment of carboxymethylcellulose and 32% dextran 70 for prevention of adhesions in rabbit uterine horn model. Int J Fertil 1988;33:278–82.
[4] Linsky CB, Cohen SM, Franklin RR, Haney AF, Malinak LR, Patton GW, Rock JA, Rosenberg SM, Webster BW, Yuzpe AA. Prevention of postsurgical adhesions by INTERCEED(TC7), an